Construction and Building Materials 250 (2020) 118865

Contents lists available at ScienceDirect

Construction and Building Materials

journal homepage: www.elsevier.com/locate/conbuildmat

Effect of MgO, Mg-Al-NO_3 LDH and calcined LDH-CO_3 on chloride resistance of alkali activated fly ash and slag blends

Tao Liu [a,b], Yuxuan Chen [a,b], Qingliang Yu [b,c,*], Jianfeng Fan [d], H.J.H. Brouwers [a,b]

[a] *State Key Laboratory of Silicate Materials for Architectures, Wuhan University of Technology, Wuhan 430070, PR China*
[b] *Department of the Built Environment, Eindhoven University of Technology, 5600MB, Eindhoven, the Netherlands*
[c] *School of Civil Engineering Wuhan University, Wuhan 430072, PR China*
[d] *School of Civil Engineering and Architecture, Wuhan University of Technology, Wuhan 430070, PR China*

HIGHLIGHTS

- The incorporation of MgO, LDH-NO_3 and CLDH delays the reaction rate.
- The MgO improves the microstructure and compressive strength of AAFS blends.
- The CLDH rebuilds the LDH phase and refines the microstructure of AAFS blends.
- The MgO, LDH-NO_3 and CLDH improve the chloride resistance of AAFS blends.

ARTICLE INFO

Article history:
Received 26 November 2019
Received in revised form 6 March 2020
Accepted 22 March 2020

Keywords:
Alkali activated slag/fly ash
layered double hydroxides (LDHs)
Magnesium oxide (MgO)
calcined layered double hydroxides (CLDHs)
Chloride resistance
Reaction kinetics
Pore structure
Compressive strength

ABSTRACT

The mechanism of layered double hydroxides (LDHs) formation with the addition of magnesium oxide (MgO), the LDHs reconstruction of calcined layered double hydroxides (CLDHs) and the effect of externally added synthetic LDHs in alkali-activated materials (AAMs) system are the important factors influencing the chloride resistance of AAMs. The objective of this research is to investigate the different effects of MgO, nitrate intercalated LDH (Mg-Al-NO_3 LDH) and calcined natural LDH-CO_3 on the alkali activated fly ash and slag blends (AAFS) in terms of chloride resistance. Mg-Al-NO_3LDH was successfully synthesized with the co-precipitation method. CLDH was also obtained by thermal treating natural Mg-Al-CO_3 LDH. The reaction heat flow and reaction products of the AAFS were tested by isothermal calorimetry and X-ray diffraction (XRD), respectively. The microstructure of the AAFS was characterized by the nitrogen sorption tests (BET) and mercury intrusion porosimetry (MIP). The compressive strength of AAFS was also tested. The non-steady-state migration (NSSM) was applied to determine the chloride resistance of AAFS. The Ordinary Portland Cement (OPC) samples were also studied for comparative purpose. The results of the calorimeter test showed that the MgO, Mg-Al-NO_3 LDH, and CLDH delayed the time to reach the reaction peak (TRRP) at 3.9%, 11.2%, and 9.2%, respectively. The MIP results illustrated that mesopores and micropores of AAFS were refined by the three admixtures. The NSSM results indicated that CLDH can significantly improve the chloride resistance of AAFS binder comparing to the samples containing MgO and Mg-Al-NO_3 LDH. The different influences of MgO, Mg-Al-NO_3 LDH and CLDH were compared in this study.

1. Introduction

Numerous military and civilian concrete structures exposed to the marine environment face the risk of chloride corrosion [1]. Chloride penetration into reinforced concrete can cause local destruction of the passive layer, leading to localized corrosion. Consequently, the usability and load-bearing capacity decreased, even the failure of the structure could occur. Facing a large amount of chloride ingress problems, approximately 3.4% of the global GDP ($2.5 Trillion USD) is spent each year to prevent, mitigate, and repair the infrastructure damage due to chloride-induced corrosion [2]. As we can see from Fig. 1, remarkable chloride ingress problems are universal worldwide [3]. The corrosion problems of offshore concrete structures lead to an urgent demand for the research about the chloride resistance of the alkali activated materials (AAMs). The effect of the alkaline environment in AAMs on

---

* Corresponding author at: Department of the Built Environment, Eindhoven University of Technology, 5600MB, Eindhoven, the Netherlands.

E-mail address: q.yu@bwk.tue.nl (Q. Yu).

https://doi.org/10.1016/j.conbuildmat.2020.118865
0950-0618/© 2020 The Author(s). Published by Elsevier Ltd.

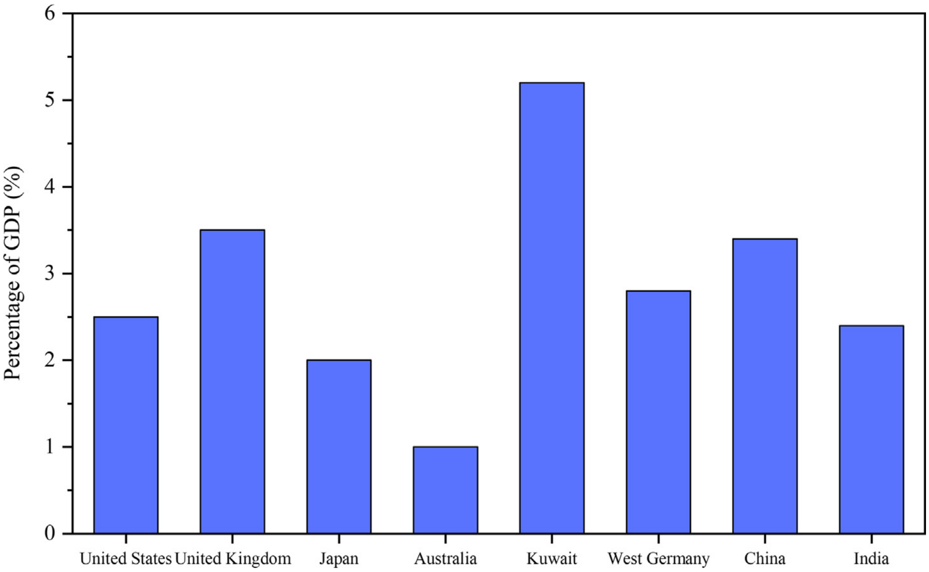

Fig. 1. Cost of corrosion related to GDP in different countries [3].

passivate steel bars may be very important in improving the durability of the reinforced concrete structure. Meanwhile, the use of by-product in AAMs also meet the demand for sustainable development worldwide. To solve these issues, many methods were developed to prevent chloride penetration. Table 1 illustrates the investigations by diverse researches subjected to chloride resistance.

Recently, Layered double hydroxides (LDHs) are widely investigated to absorb undesired anions in aqueous solution [18]. LDHs are one of the primary reaction products in alkali activated slag. The skeleton of LDHs consists of the divalent metal ion and trivalent metal ion, for example, Mg^{2+} and Al^{3+} [19]. The interlayer of LDHs has the capability of binding the anions in AAMs, for instance, chloride ions and sulfate ions. The interlayer anion can exchange with other anions and the affinity order of anion is characterized by Costa [20] as:

$$CO_3^{2-} > SO_4^{2-} > OH^- > F^- > Cl^- > Br^- > NO_3^- \quad (1)$$

Thus, the amount of Mg-Al-NO_3^--LDH influences the chloride resistance in the silicate matrix, because the NO_3^- can exchange the Cl^- in the chloride environment. Xu et al. [21] prepared the Mg-Al-NO_3^--LDH and Mg-Al-NO_2^--LDH by the co-precipitation method, and both Mg-Al-LDHs exhibited the excellent chloride removal and corrosion inhibition capacities. Qu et al. [22] reported that the finer particle size of the Ca-Al-NO_3^--LDH enhanced the

Table 1
Durability investigations of AAMs in terms of chloride resistance.

Standards	Precursors	Activators	Admixtures	Remarks	Year	Ref.
ASTM C1202	Slag	NaOH + Na_2SiO_3	Phosphoric acid	Dosage of Na_2O and H_3PO_4 of additional mixture optimize the properties and durability of samples.	2012	[4]
ASTM C1202	Slag + Metakaolin	NaOH + Na_2SiO_3	–	Increased metakaolin contents and higher activator concentrations decrease the water sorptivity and chloride permeability.	2012	[5]
ASTM C1202	Slag	NaOH + Na_2SiO_3	Nano-silica, Micro-silica	The micro-silica admixture increases the chloride resistance, but the nano-silica shows the opposite results.	2017	[6]
ASTM C1202	Slag + Fly Ash	Na_2SiO_3	–	The chloride resistance sequence of the different precursors: Slag > OPC > Fly Ash.	2018	[7]
ASTM C1202	Slag + Fly Ash	NaOH + Na_2SiO_3	MgO	The increasing incorporation of MgO promotes hydrotalcite formation and chloride resistance.	2018	[8]
ASTM C1543	Slag + Fly Ash	Na_2SiO_3	–	The surface area of production gel increases with the fly ash inclusion, and the chloride sorption is increased.	2013	[9]
ASTM C1556	Slag + Fly Ash	NaOH + Na_2SiO_3	–	Fly ash mortars are much more susceptible to the chloride environment than the OPC mortars.	2016	[10]
ASTM C1556	Slag + Fly Ash	NaOH + Na_2SiO_3 or KOH + Na_2SiO_3	–	High calcium content increases the chloride resistance, but the high alkali concentration has the opposite effect.	2018	[11]
ASTM C1556	Fly Ash	NaOH + Na_2SiO_3 + $Na_2Si_2O_5$	–	The chloride diffusion resistance of the FA-based concrete is very low.	2019	[12]
NT Build 443	Slag	NaOH + Na_2SiO_3	–	The relationships of chloride diffusion factors are related to water soluble chloride.	2019	[13]
NT Build 443	Slag + Fly Ash	NaOH + Na_2SiO_3	–	The pH value affects the chemical and physical chloride binding capacity from the long term chloride exposure.	2019	[14]
NT Build 492	Slag	NaOH + Na_2SiO_3	–	The increasing Ms promotes the chloride resistance.	2013	[15]
NT Build 492	Slag	Na_2CO_3	CLDH	The CLDH admixture enhances the chloride binding capacity of the sodium carbonate activated slag	2017	[16]
NT Build 492	Slag + Fly Ash	NaOH + Na_2SiO_3	–	The increase of Ms and decrease of fly ash content reduce the chloride diffusion due to the optimization of microstructure.	2019	[17]

chloride resistance of the cement matrix, which is attributed to both the physical barrier effect of the increased tortuosity and chemical binding capacity of the LDHs. Regardless of the references mentioned above, the synthesis pH of LDH, flow rates, temperature, pressure environment partly contribute to the property of the final product [23]. However, few literature reports the externally added synthetic LDHs in AAMs pertaining to chloride resistance [2]. Thus, there are still largely unknown areas in terms of LDHs applied in AAMs matrix to promote the chloride resistance. The influence of the synthetic and externally added LDHs in AAMs needs to be deeply investigated.

Magnesium oxide (MgO) is introduced in the AAMs to deal with the chloride ingress problem, because the MgO content in the silicate system influences the formation of LDHs in the AAMs matrices, thus improving chloride resistance [8]. High contents of MgO (higher than 8 wt%) increase the formation of the hydrotalcite-like phase and decrease the C–S–H phase. Consequently, the chemical binding capacity increases by more LDHs content but the physical binding capacity decreases by the less C–S–H gel [24]. With the addition of MgO in AAMs, it is hard to control the content of LDHs formation, because the reaction is affected by many parameters, e.g. the two metal ions molar ratio [25]. Therefore, further investigations are needed for a desirable control of MgO content in AAMs to increase the chloride binding capacity.

The calcined layered double hydroxides (CLDHs) can be calcined from the natural hydrotalcite (Mg-Al-CO_3 LDH) and rebuild the layered double structure in the high alkaline system [26]. Sato et al. [27] investigated the effect of CLDH on the cement concrete structure, the results of the rapid chloride penetration test showed that the CLDH promoted the chloride binding capacity due to the reconstruction of a LDH-like phase in the cementitious matrix (Fig. 2). The utilization of the CLDH in the sodium carbonate activated slag exhibited a higher chloride resistance than the reference samples without CLDH incorporation [28]. CLDH rebuilds the LDH-like phase to absorb the chloride ion and increases the chemical chloride binding capacity. Therefore, CLDH enhances the physical absorption of chloride ions. CLDHs has the potential to act as an effective chloride adsorbent in AAMs matrix. The CLDH content promotes the LDH-like phase formation, thereby affecting the chloride binding capacity of AAMs. As mentioned above, there were studies about applying CLDHs in sodium carbonate activated slag, but very limited researches about CLDHs applied in alkali activated slag and fly ash. Consequently, investigations on chloride adsorption of CLDHs are needed to understand the influence of the CLDHs dosage in alkali activated slag and fly ash.

The MgO and CLDH influence the LDH formation in AAMs, and externally added LDHs can play the role of filler and chemical absorbent in AAMs, thereby affecting the chloride resistance of AAMs. Therefore, the objective of this research is to investigate the different effects of MgO, nitrate intercalated LDHs and calcined LDH-CO_3 on chloride resistance of the AAFS binder. The reaction heat flow, reaction products, pore structures, mechanical properties and chloride resistance of alkali activated fly ash and slag incorporated with MgO, LDHs, and CLDHs are investigated. Furthermore, the mechanism to form the LDH in AAFS affected by MgO and CLDH is analyzed. The Ordinary Portland Cement (OPC) based samples are also used as the comparison to the AAMs samples. The respective contributions to enhance the chloride resistance of the three admixtures are evaluated.

2. Experiments

2.1. Starting materials

Class F fly ash (FA), ground granulated blast-furnace slag (GGBS) and Enci Portland Cement CEM Ⅰ 52.5 R were utilized in this research. The chemical compositions were determined by X-ray fluorescence (XRF), as shown in Table 2.

The MgO utilized in this study was Magnesia 291 (provided by the MAGNESIA GERMANY) with a purity of 96%. The reactivity of the MgO was tested by the reaction time with acetic acid following [29]. The reaction time was 19.86 s, which was defined as a medium active magnesia. The specific surface area of the MgO was 51.39 m^2/g and Fig. 3 showed the crystalline pattern of MgO.

Mg-Al-NO_3 LDH was prepared by a co-precipitation method. Solution A containing Mg $(NO_3)_2 \cdot 6H_2O$ and Al $(NO_3)_3 \cdot 9H_2O$ with Mg/Al molar ratio of 3.0 ($[Mg^{2+}] + [Al^{3+}] = 1.0$ mol/L) and solution B containing 1.75 mol/L NaOH and 0.75 mol/L $NaNO_3$ was simultaneously dripped into 50 mL deionized water in a 500 mL container with magnetic stirring under N_2 atmosphere. The pH value of the solution was maintained at 11.0 ± 0.5. Afterward, the resulting suspension was aged at 65 °C for 24 h in a thermostatic bath. The final

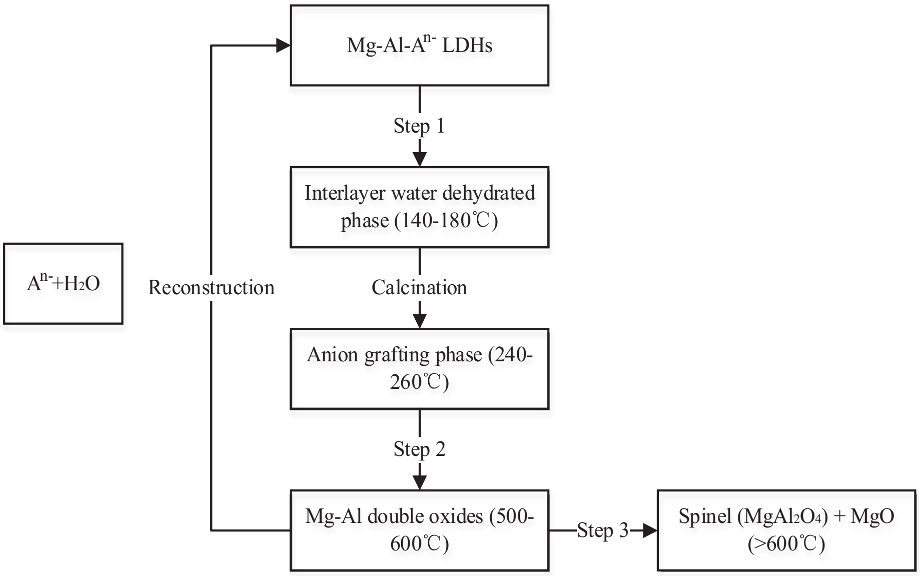

Fig. 2. Calcination and reconstruction of LDHs.

Table 2
Chemical composition of the FA, GGBS, and Cement.

Composition	MgO	Al_2O_3	SiO_2	SO_3	K_2O	CaO	TiO_2	Fe_2O_3	Cl	LOI*(%)
FA	1.137	25.576	53.892	2.905	1.601	5.441	1.503	7.883	0.062	3.79
GGBS	9.023	13.093	31.246	5.15	0.299	39.067	1.4	0.679	0.043	1
Cement	1.75	3.878	16.55	4.146	0.191	69.49	0.283	3.669	0.042	0.72

*LOI = loss on ignition at 1000 °C.

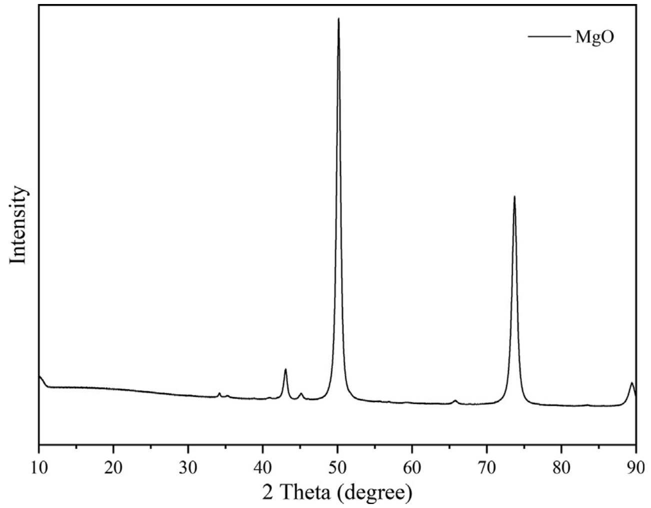

Fig. 3. X-ray diffractogram of MgO.

precipitate was filtered, thoroughly washed, and dried at 75 °C for 24 h. The set-up of the Mg-Al-NO_3 LDHs synthesis is shown in Fig. 4.

CLDH was calcined from the natural hydrotalcite (LDH-CO_3) with a heating rate of 5 °C /min and kept at 550 °C for 3 h. Then the material was cooled naturally in the furnace to 105 °C before it was moved to a sealed centrifuge tube and kept in a desiccator under vacuum. The characteristic peaks of the LDH and CLDH are presented in Fig. 5, showing the crystalline patterns of the LDH and CLDH. The feature peaks of LDH are situated at 13.6°, while the feature peaks of the CLDH were situated at 41.2°, 51.3°, and 75.6°. Fig. 5d illustrates that the CLDH shows the non-homogeneity state, which proves that the double layered structure collapsed to the non-rule layered structure.

2.2. Sample preparation

MgO, Mg-Al-NO_3 LDH, and CLDH replaced 2 wt% and 4 wt% of the alkali activated binder, which are described as modified samples. GGBS / FA mass ratio is 7:3 (see the sample ID in Table 3).

The activator used in this research was a mixture of analytical grade sodium hydroxide pellets (99% purity) and sodium silicate solution, and additional water is added to the solution to meet the requirement of liquid/solid (L/S) ratio. The SiO_2/ Na_2O molar ratio was 1.5. The composition of the sodium silicate is shown in Table 4. For the mixtures shown in Table 3, the first letter P and M represent paste sample and mortar sample, respectively. A0 represents AAMs without additional admixture, while M represents MgO, L represents LDH and C represents CLDH, and the number represents the mass content equals to binder percentage.

The starting raw materials were mixed with the designed proportion in the concrete mixer following the preparation procedure suggested by EN 196-1 [30]. Paste samples were cast in the steel molds (40 mm × 40 mm × 40 mm) followed by the vibration. All the mortar samples were cast in the Ø 100 mm × 200 mm cylinder mold followed by the vibration. The samples were all cured in the ambient temperature for intended period, e.g. 3, 7 or 28 days.

2.3. Characterization

2.3.1. X-ray diffractometry

X-ray diffractometry (XRD) was performed by using a Bruker D4 Phaser instrument with Co-Kα radiation (40 kV, 30 mA). The powdered specimens were measured with a step size of 0.05° from 10° to 90° 2θ, and the counting time was 1 s/step.

2.3.2. Isothermal calorimetry

The heat flow of the samples by different precursors were measured by an isothermal calorimeter set at 20 °C (TAM AIR Calorimetry). It was noteworthy that the initial 4–6 min after mixing could not be measured due to the sample preparation procedure and the initial 0.5–1 h of the heat flow data could be inaccurate because of the instability of apparatus disturbed by the loading process. The results were normalized by the mass of the solid, excluding the water amount.

2.3.3. Nitrogen physisorption test

The nitrogen sorption test was conducted by TriStar Ⅱ 3020, Micromeritics. The pore size distribution was determined by the Barett, Jonyer, and Halenda (BJH) method [31] from the desorption branch. Before the test, paste samples were ground to powder and the samples were immersed in the 2-propanol for 24 h to stop the

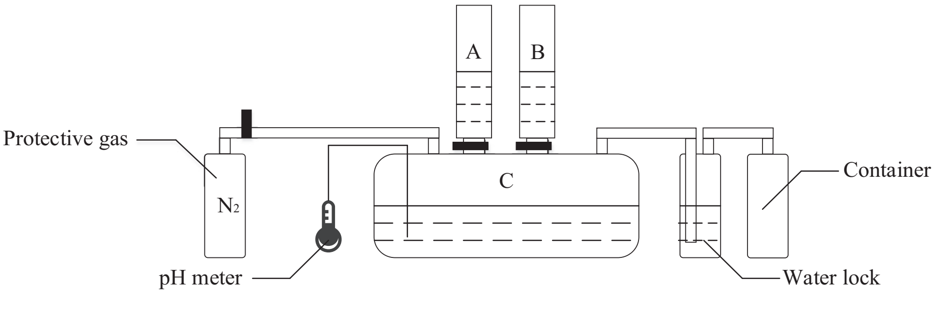

Fig. 4. Scheme of Mg-Al-NO_3 LDH synthesis process.

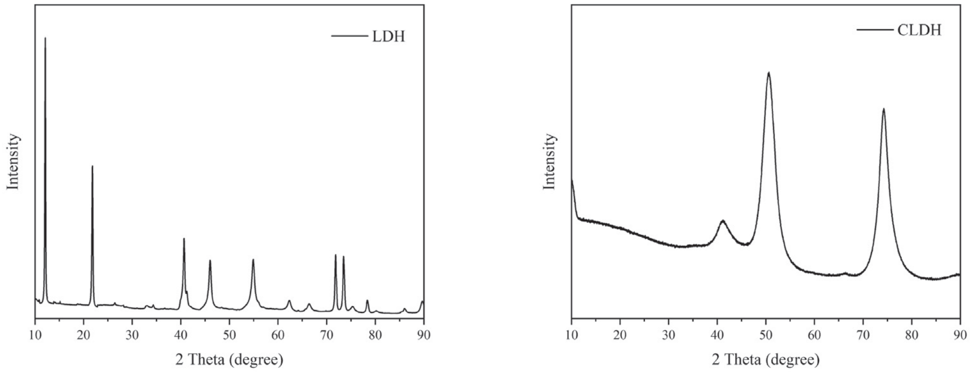

a. X-ray diffractogram of Mg-Al-NO_3 LDH

b. X-ray diffractogram of CLDH

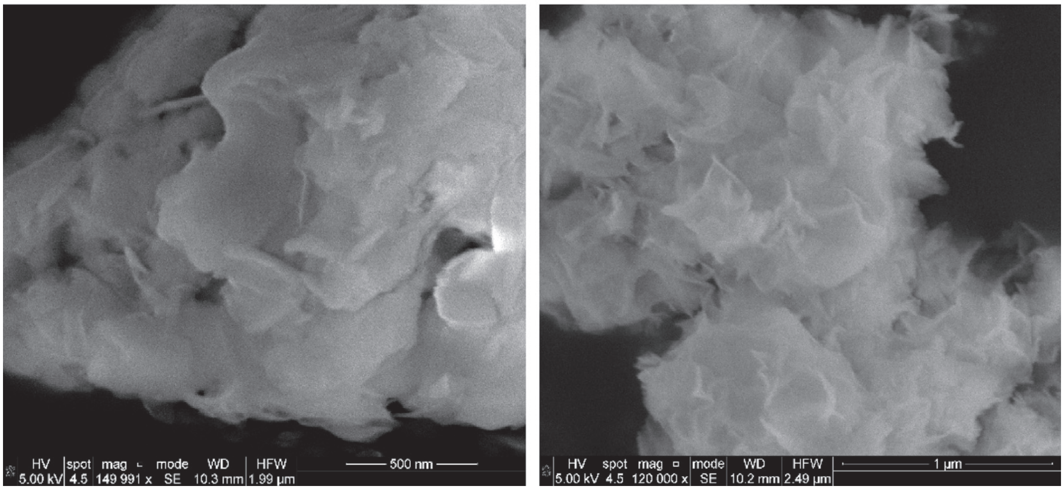

c. SEM of Mg-Al-NO_3 LDH (150000×)

d. SEM of CLDH (120000×)

Fig. 5. XRD pattern and morphology of Mg-Al-NO_3 LDH and CLDH.

Table 3
Formulations of the pastes and mortars using different additions.

Sample ID	Solid (wt. %)						Sand (wt. %)	Na_2O/Solid (wt. %)	L/S*
	GGBS	FA	MgO	Mg-Al-NO_3 LDH	CLDH	Cement			
P-A0	70	30	–	–	–	–	–	7%	0.4
P-M2	68.6	29.4	2	–	–	–	–	7%	0.4
P-M4	67.2	28.8	4	–	–	–	–	7%	0.4
P-L2	68.6	29.4	–	2	–	–	–	7%	0.4
P-L4	67.2	28.8	–	4	–	–	–	7%	0.4
P-C2	68.6	29.4	–	–	2	–	–	7%	0.4
P-C4	67.2	28.8	–	–	4	–	–	7%	0.4
P-OPC	–	–	–	–	–	100	–	–	0.4
M-A0	70	30	–	–	–	–	300	7%	0.4
M-M2	68.6	29.4	2	–	–	–	300	7%	0.4
M-M4	67.2	28.8	4	–	–	–	300	7%	0.4
M-L2	68.6	29.4	–	2	–	–	300	7%	0.4
M-L4	67.2	28.8	–	4	–	–	300	7%	0.4
M-C2	68.6	29.4	–	–	2	–	300	7%	0.4
M-C4	67.2	28.8	–	–	4	–	300	7%	0.4
M-OPC	–	–	–	–	–	100	300	–	0.4

* L/S = Liquid/Solid mass ratio (where solid is defined as FA + GGBS + MgO/ Mg-Al-NO_3 LDH /CLDH).

hydration process, then dried to constant weight at the age of 28 days. The pastes were degassed at 120 °C for 4 h prior to the nitrogen physisorption test as the sample pretreatment. Then, the pastes were put in TriStar Ⅱ 3020, Micromeritics, and the sample testing tubes were immersed in liquid nitrogen to cool down to temperature of nitrogen boiling point.

Table 4
Chemical composition of the sodium silicate.

	SiO_2	Na_2O	H_2O
Wt. %	27.69%	8.39%	63.92%

2.3.4. Mercury intrusion porosimetry

The samples for the mercury intrusion porosity (MIP) analysis were selected from mortars, with the dimensions ranging of 3–5 mm. The selected samples were immersed in the 2-propanol for 24 h to halt the hydration process and then put in the vacuum drying oven for 3 days in order to remove all the pore water. The MIP tests were conducted by using a Micromeritics Autopore 9600 Mercury Porosimeter.

2.3.5. Compressive strength

After 28 days of curing, the strength of the samples was determined according to EN 196-1 [30]. The samples were centered on the platens of the machine. Subsequently, the load was increased smoothly at the rate of 2400 N/s over the entire load application until the fracture load.

2.3.6. Non-steady-state migration experiments

The Ø 100 × 200 mm cylindrical mortars were cast and cut into 50 ± 2 mm thick slice. The cylindrical samples were put in the vacuum container for vacuum treatment for 3 h with the pressure in the range of 10–50 mbar (1–5 kPa), with the vacuum pump still running, then the samples were immersed in the saturated $Ca(OH)_2$ solution for 18 ± 2 h. Subsequently, the non-steady-state migration (NSSM) experiments were carried out according to the NT Build 492 [32].

After the NSSM experiments, the samples were split along the diameter of cylindrical surface into two part to expose the inner faces. Subsequently, the $AgNO_3$ solution was sprayed on the split surface, AgCl (white precipitation) was formed on the surface to reveal the chloride penetration depths. The non-steady-state migration coefficient was calculated by [32]:

$$D_{nssm} = \frac{0.0239(273+T)L}{(U-2)t}\left(x_d - 0.0238\sqrt{\frac{(273+T)L\cdot x_d}{U-2}}\right) \tag{2}$$

where:

D_{nssm}:	non-steady-state migration coefficient, $\times 10^{-12}$ m^2/s;
U:	the absolute value of the applied voltage, V;
T:	the average value of the initial and final temperatures in the anolyte solution, °C;
L:	the thickness of the specimen, mm;
x_d:	the average value of the penetration depths, mm;
t:	test duration, hour.

The scheme of the NSSM test set up is shown in Fig. 6.

3. Results and discussion

3.1. Reaction kinetics

The reaction process of AAFS (shown in Fig. 7a) can be generally classified into three stages [33,34]: (a) destruction–coagulation;

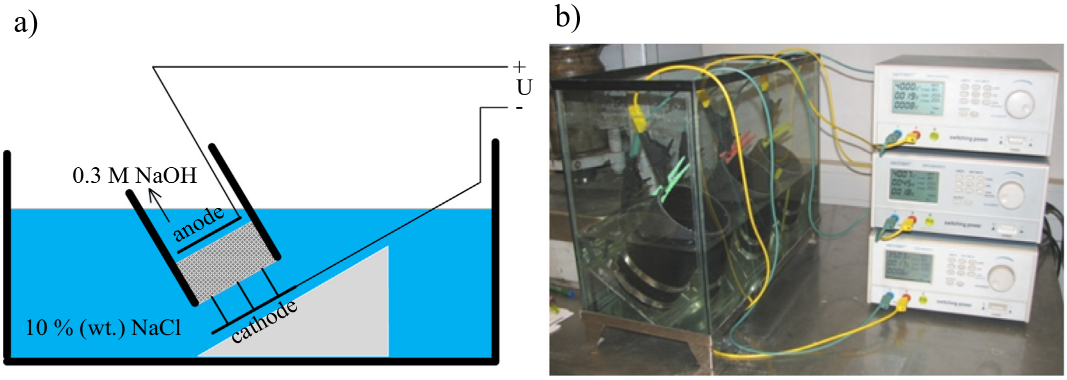

Fig. 6. NSSM test set-up: a) schematic, b) test setup.

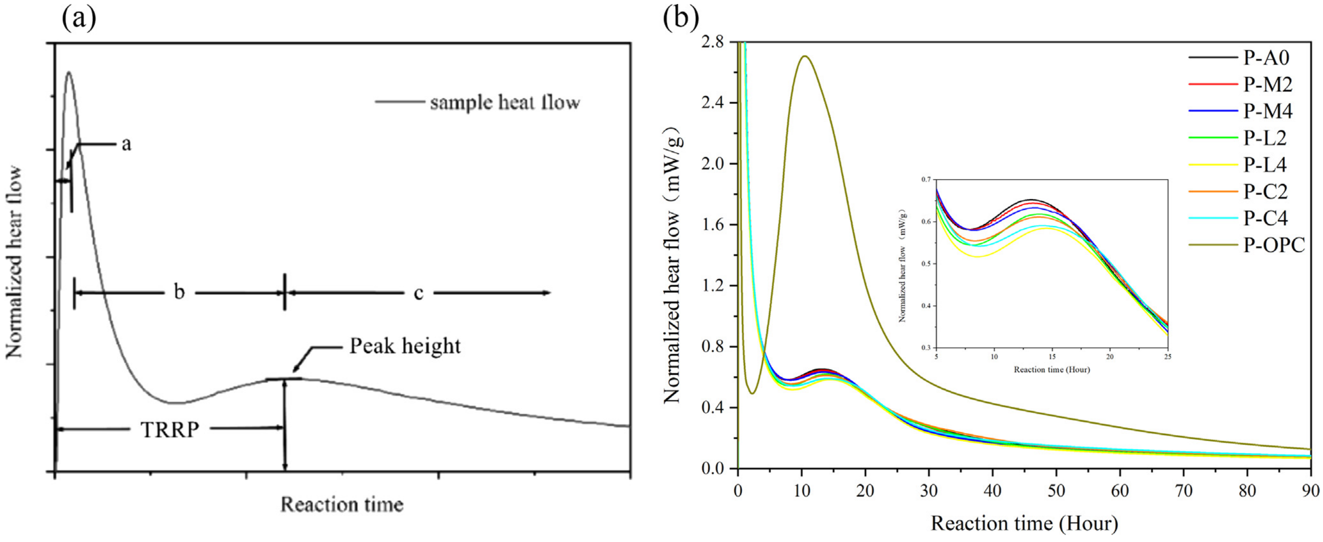

Fig. 7. Normalized reaction heat flow: a) hydration process of AAFS pastes, b) AAFS and OPC pastes.

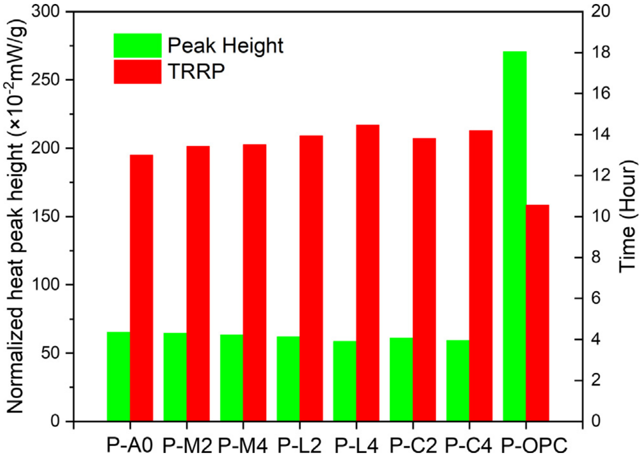

Fig. 8. Heat peak and TRRP of AAFS and OPC pastes.

(b) coagulation–condensation; (c) condensation–crystallization. The normalized hydration heat flows of different samples are shown in Fig. 7b. The MgO, LDHs and CLDHs addition exhibit a prolonged dormant period and the time to reach the reaction peak (TRRP) of the investigated mixture ranged from 10 to 15 h (shown in Fig. 8).

The primary differences between OPC pastes and AAFS pastes are obvious. The normalized hydration heat peak of the AAFS binder is 75.90% smaller than that of the OPC binder, comparing to the P-OPC and the P-A0 (Fig. 8). It is clear from Fig. 8 that increasing the MgO, LDHs and CLDHs content slightly prolong the TRRP.

Due to the high MgO content in the P-M2 and P-M4 (higher than 8 wt%), the high MgO systems can preferentially form hydrotalcite by reacting Al with Mg [24], and the hydration heat shows the prolonged TRRP. As shown in Fig. 7b and Fig. 8, the P-M2 and P-M4 extend the TRRP at 3.2% and 3.9% comparing to the P-A0, respectively. Firstly, MgO dissolve in the solution and release Mg^{2+}; Then, the free Mg^{2+} react with the OH^- in the alkaline environment forming the $Mg(OH)_2$ precipitation and decreased slightly the pH value. Consequently, the MgO addition increases the TRRP and delays the hydration process slightly. Meanwhile, the increased MgO content has a slight effect on TRRP in the high MgO (higher than 8 wt%) and Al_2O_3 (higher than 14 wt%) blended system [35].

The addition of LDHs in the geopolymer pastes shows a slight prolonged TRRP and decreased heat peak. The P-L2 and P-L4 exhibit the 7.2% and 11.2% delay comparing to the P-A0 reference, respectively. Firstly, the nitrate ion in the LDH releases some NO_3^-, and the OH^- in the AAFS matrix partly exchange with NO_3^-, resulting in the pH value decrease of the AAFS matrix. Thus, it delays the TRRP. Secondly, the agglomeration of LDH materials can also extend the TRRP in AAFS matrix. Therefore, the incorporation of LDH exhibit a decrease in TRRP and reaction heat peak.

Ke et al. [28] utilized the CLDHs to expedite the reaction kinetics of the different Na_2CO_3 activated blast furnace slags. The CLDHs was associated with the removal of dissolved CO_3^{2-} from the fresh cement, yielding a rise in the pH value, and the potential seeding effects. While the CLDHs in sodium silicate and sodium hydroxide activated fly ash and slag system demonstrate the opposite effect, the CLDHs react withOH^-, forming the LDH-OH and yielding a decrease in the pH value, consequently prolonging the TRRP. Therefore, the TRRP prolongs 0.81 h (P-C2) and 1.19 h (P-C4) comparing to the reference group P-A0 (shown in Fig. 8), which extends the TRRP 6.2% and 9.2%, respectively.

3.2. Reaction products

The XRD patterns of the samples show that the primary hydration products of AAFS binder are C-S-H, hydrotalcite-like phase, and Mullite.

Fig. 9a) and b) show the crystalline phases in all the AAFS samples exhibit the same reaction products at 3 curing days and 28 curing days, respectively. Comparing Fig. 9 a) and b), the 3-day crystalline products of AAFS are practically consistent with the 28-day crystalline products. The primary AAFS crystalline products are formed in the initial 3 days. The observed results are consistent with the results presented in section 3.1, that the primary reaction heat flows and products are formed in the early stage. However, the OPC samples show the peak changes between 3 days and 28 days, which illustrates that the hydration still goes on after 3 days.

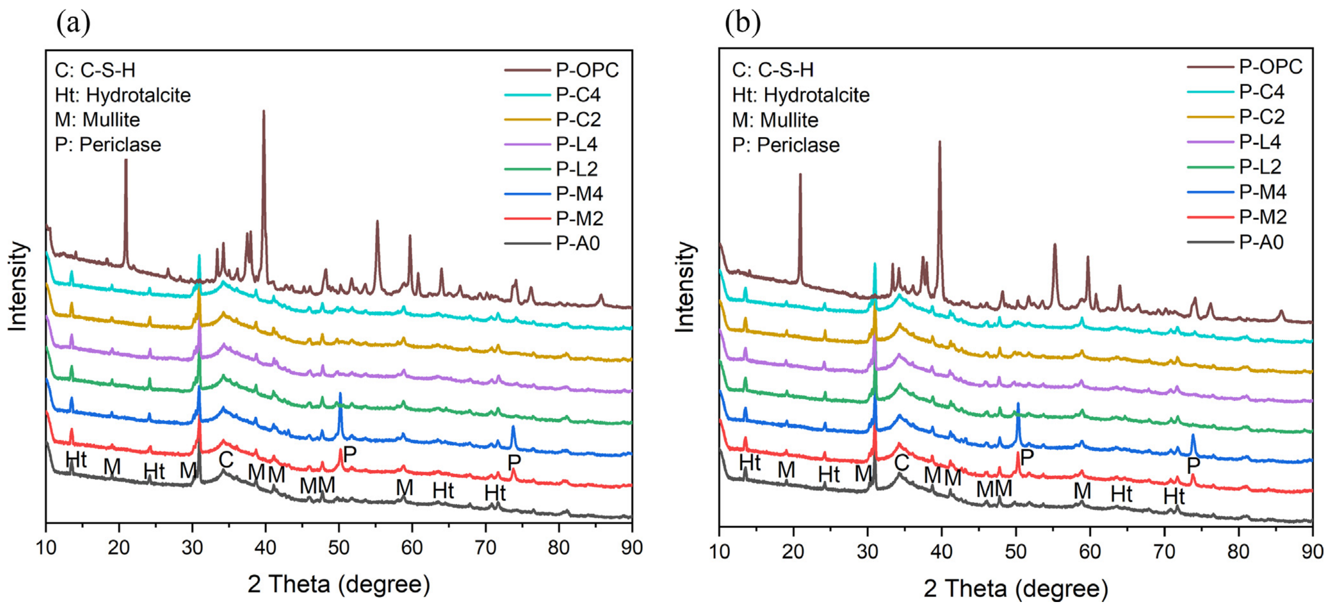

Fig. 9. XRD patterns of AAFS and OPC pastes at a) 3 days, b) 28 days.

The main characteristic peak of hydrotalcite is identified at 13.6° from Fig. 9a) and b). However, Ke et al. [36] reported the main peak of the XRD pattern for a similar hydrotalcite-like phases after filtration was centered at 11.6°. The shift in the hydrotalcite-like peak can be attributed to the partial carbonation of the LDH.

Periclase is identified in specimens prepared with MgO addition (P-M2 and P-M4), which indicated that the MgO is not fully reacted with slag to form LDH. However, according to the previous study [8], the content of LDH formed from MgO in AAFS binder has the potential to grow over time, due to the solid state reaction of MgO in alkali activated cement.

The XRD patterns of P-L2, P-L4, P-C2, and P-C4 demonstrate almost the same intensity of LDHs. The characteristic peak of the CLDH phase is not found either in 3-day or 28-day XRD patterns, while the peak of the hydrotalcite-like phase appears, proving the CLDH completes the reconstruction process in AAFS to form the LDH.

Combining Fig. 9a) and b), the MgO and CLDH participate in the LDH formation in the AAFS matrix. Meanwhile, the externally added LDH can remain in the AAFS matrix. The three admixtures show the same results in the AAFS matrix in terms of the crystalline products.

3.3. Pore structure

As seen in Fig. 10a, the OPC pastes obtain the most mesopores (20–50 nm) and macropores (50–100 nm) and the lowest micropores. Meanwhile, the AAFS pastes are also the highest in mesopores and the lowest in micropores and macropores, as shown in Fig. 10b. The amount of the mesopores are nearly the same for all the AAFS pastes, which are quite different from the mesopores in OPC pastes. OPC pastes show a larger pore size than those of AAFS pastes.

Fig. 10b shows the pore size distribution of AAFS pastes incorporating 2 wt% and 4 wt% MgO, LDH and CLDH. It shows the porosity slightly increases from the reference sample P-A0 to samples containing 2 wt% and 4 wt% MgO and CLDH. Furthermore, the porosity decreases with the LDH addition. Therefore, the pore size distribution is slightly improved by the LDH addition and the microstructure is refined.

The pore size distribution results of mortars from the MIP measurement are shown in Fig. 11. It is obvious that the pore size distribution of OPC mortars mainly situates between the 10–100 nm (mesopores and macropores), which are consistent with the BJH method results shown in Fig. 10a.

The AAFS mortars are the highest in mesopores and the lowest in macropores. As described in Fig. 11b, the addition of MgO (M-M2 and M-M4) increases the total volume of the macropores comparing to the reference M-A0. However increasing the content of MgO can reduce the mesopores of AAFS mortars, which forms a small amount of the $Mg(OH)_2$ to fill the pores and corresponds well with the reference [37,38].

Fig. 12 and Fig. 13 show the cumulative porosity and the total porosity of AAFS and OPC samples. The total porosity of OPC mortars (20.01%) is much higher than the M-A0 mortars (3.969%).

The porosity of AAFS decreases with the increasing MgO dosage, which is generally in agreement with the BJH method result (Fig. 10 b). The LDH admixture in the AAFS samples also shows a slight influence on the porosity, but the 2 wt% and 4 wt% replacement of the fly ash and slag exhibit little difference in terms of the porosity (4.64% and 4.57%, respectively). However, comparing the porosity of P-A0, the incorporation of 2 wt% and 4 wt% CLDH (M-C2 and M-C4) has a positive correlation on total porosity, increasing up to 4.35% and 4.87%, respectively.

In general, the incorporation of MgO, LDH, and CLDH have slight effects on total porosity, while the unreacted MgO functions as the inert filler in the AAFS matrix. The LDH and CLDH admixtures have a slight effect on the microstructures. The AAFS mortars exhibit almost the same porosity, ranging from 3.96% to 4.93%.

Combining the nitrogen sorption results and MIP measurement results, the pore size of AAFS mortars mainly range from 3 to 10 nm (mesopores), while the pore size of OPC mortars mainly widely situate from 10 to 100 nm (both mesopores and macropores) The total porosity of the AAFS mortars are from 3.96% to 4.93%, while the OPC mortars is around 20.01%.

3.4. Compressive strength

Fig. 14 shows the compressive strength of the AAFS and OPC pastes at the curing age of 3, 7 and 28 days. Fig. 15 shows the relative strength of blended pastes at 3, 7 and 28 days compared to the AAFS (P-A0). The increasing trend of compressive strength shows that the strength of AAFS samples may continue to increase after the 28-day curing time, due to the incorporation of fly ash

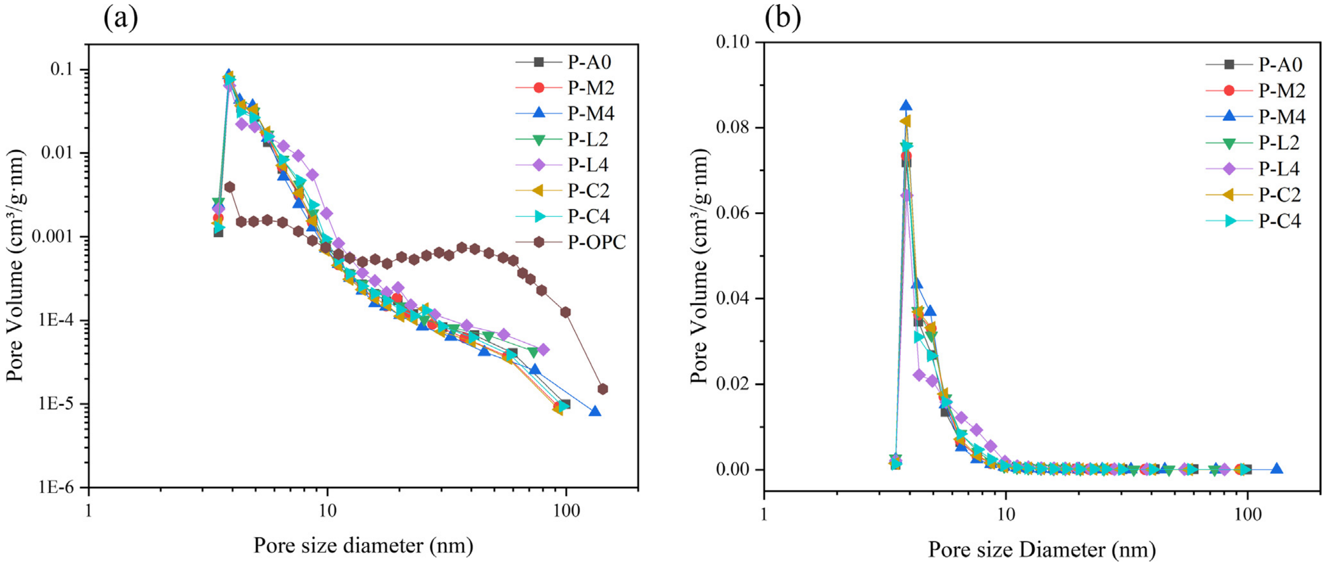

Fig. 10. Pore size distribution of AAFS and OPC from nitrogen sorption results: a) AAFS and OPC pastes, b) AAFS pastes.

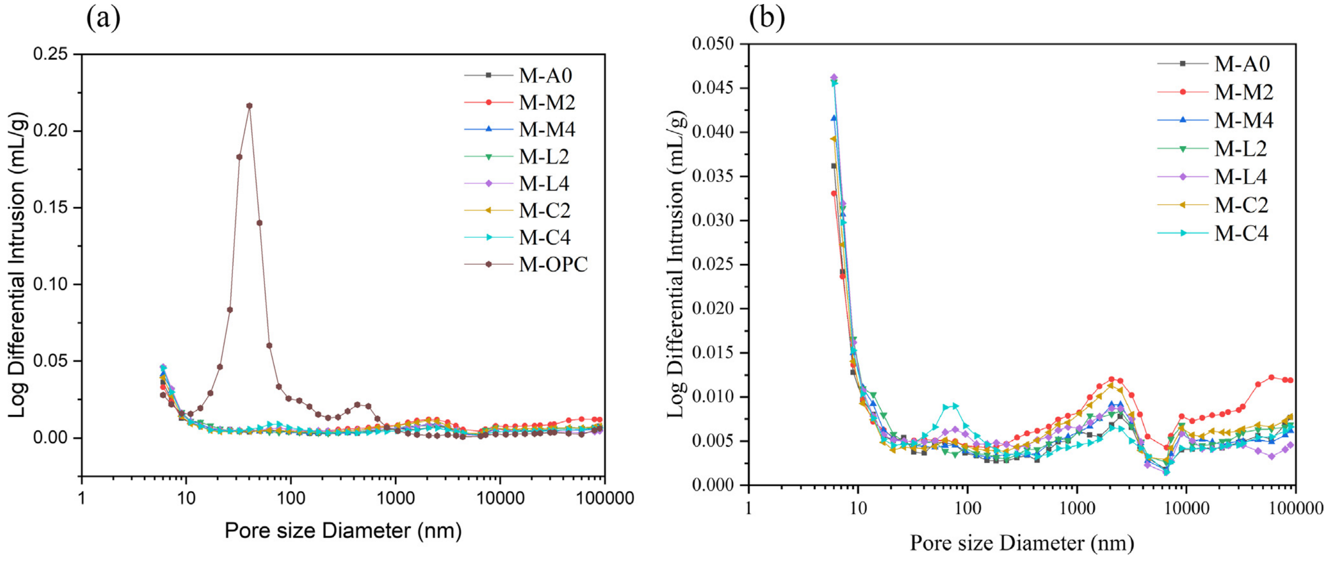

Fig. 11. Pore size distribution of AAFS and OPC from MIP results: a) AAFS and OPC mortars, b) AAFS mortars.

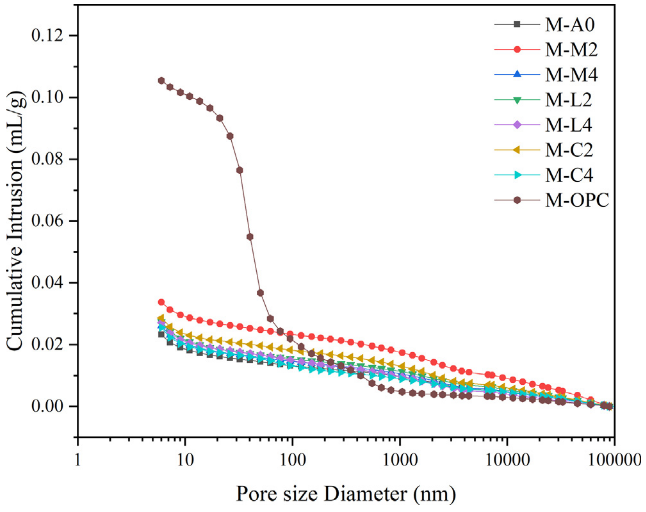

Fig. 12. Cumulative porosity of AAFS and OPC from MIP results.

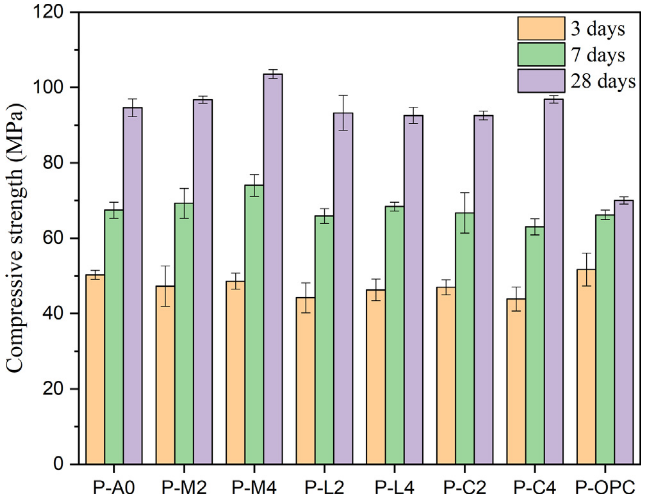

Fig. 14. Compressive strength of AAFS and OPC pastes.

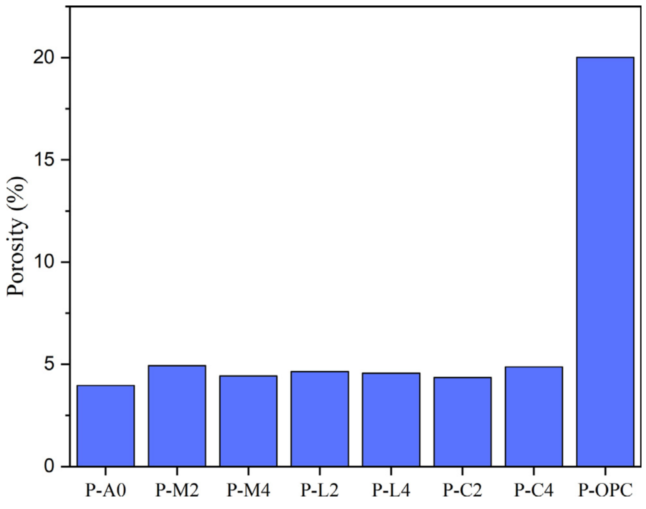

Fig. 13. Porosity of AAFS and OPC from MIP results.

with a slow pozzolanic reactivity. These observed trends are related to the XRD results shown in section 3.1, and also in agreement with [39,40].

The compressive strength increases with the increasing content of the MgO, and this agrees with previous researches [41–43]. P-M2 and P-M4 exhibit higher compressive strength than other samples, up to 96.75 MPa and 103.58 MPa at 28 days curing age, respectively. The increase in relative strength for increased MgO content is attributed to the total content of MgO. Hwang et al. [43] reported that the content of MgO at 12 wt% (including the MgO inside binder material) in alkali activated slag showed the highest compressive strength. As the MgO dosage increases in P-M2 and P-M4, the compressive strength increases. The observed results agree with the mesopores distribution shown in Section 3.3, and the increased MgO content decreases the macropores and porosity that leads to the higher compressive strength.

Increasing the dosage of LDH in AAFS shows a slight decrease in compressive strength at 28 days, compared to the reference sample (P-A0). According to [44], the strength of the concrete samples gradually decreased with the increasing content of LDH. Meanwhile, the macropores of LDH samples increased with the rising

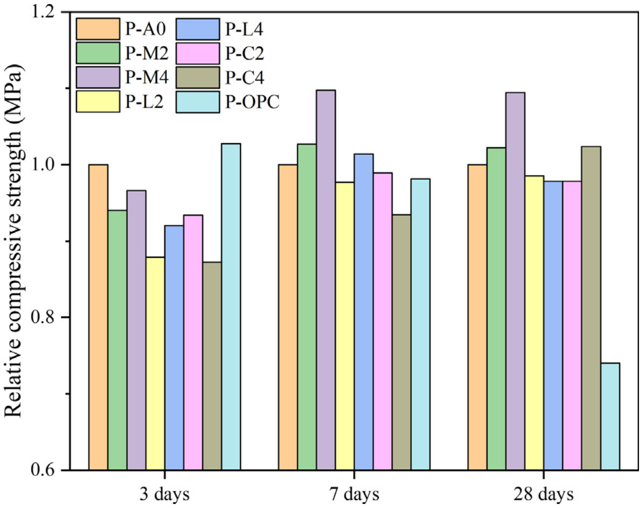

Fig. 15. Relative compressive strength of AAFS and OPC pastes.

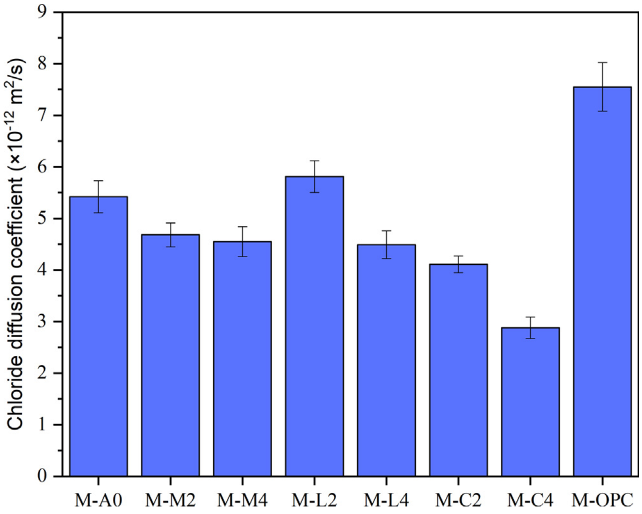

Fig. 16. Chloride migration coefficients of AAFS and OPC mortars.

dosage of LDH in Section 3.3, the obtained compressive strength is consistent with these results.

The compressive strength development of CLDH addition in AAFS exhibits the same trend with LDH addition samples, namely the CLDH addition in AAFS slightly declines the compressive strength. Furthermore, P-C2 and P-C4 show the same compressive strength level with P-L2 and P-L4, at the 28 days curing age, respectively. The observed results are in agreement with [45], who reported that the CLDH content higher than 1 wt% resulted in the reduction of compressive strength.

3.5. Chloride migration

The results of the NSSM experiments are shown in Table 5 and Fig. 16. The OPC reference illustrates the highest coefficient D_{nssm} among all mortar specimens. Meanwhile, the AAFS reference (M-A0) also shows the highest coefficient D_{nssm} in all AAFS mortars, excluding the samples with 2 wt% LDH replacement (M-L2). Fig. 17 shows the relationship between replacing materials content and chloride migration coefficients. With the increasing replacement content, the MgO, LDH and CLDH mortars show the decreasing trend of the coefficient. In general, the incorporation of MgO, LDH, and CLDH increases the chloride resistance of AAFS mortars.

As one can see from Fig. 16 and Fig. 17, the MgO admixture decreases the chloride migration coefficient. The chloride binding capacity is due to (1) the LDH phase in the AAFS [8,46,47] and (2) pore size distribution [48–50]. On the one hand, the XRD pattern (in Section 3.1) shows that the hydrotalcite phase is formed in the AAFS samples, which can increase the chloride binding capacity. The MgO is a significant resource to form the LDH, and the chloride migration coefficient proves that the MgO addition enhances the hydrotalcite formation and then promotes the chloride resistance of AAFS [8]. The results in Table 5 illustrates that the coefficient D_{nssm} of M-A0, M-M2, and M-M4 are 5.42, 4.68 and 4.55 $\times$ 10^{-12} m^2/s, respectively. The chloride migration coefficient declines by 13.7% (sample M-M2) and 16.1% (sample M-M4), compared to the reference sample M-A0. On the other hand, the pore size distributions have a large effect on the chloride resistance of the AAMs samples with supplementary cementitious materials (SCMs), especially the mesopores and macropores affect significantly the permeability of concrete. The relationship between microstructure and permeability is investigated by many researchers [17,51]. As we can conclude from Section 3.3 that the increasing MgO content leads to the lower mesopores and macropores, thus the observed results are consistent with the NSSM test.

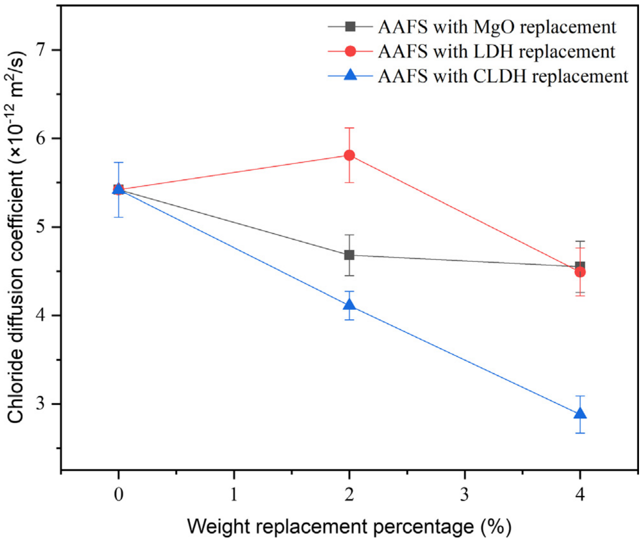

Fig. 17. The relationship between replacing materials content and chloride migration coefficient.

Fig. 16 and Fig. 17 also show the nitrate intercalated LDH incorporation in the AAFS matrix in terms of the chloride resistance. Comparing M-L2 and M-L4 to M-A0, the chloride migration coefficient of M-L2 is higher than the reference M-A0 at 7.2%, while the coefficient of M-L4 is lower than the reference sample at 17.2%. The obtained results indicate that the nitrate intercalated LDH has a remarkable increase in the chloride binding capacity of AAFS with

Table 5
Chloride migration coefficients calculated from the NSSM test in the mortar at 28 days curing age.

Sample ID	M-A0	M-M2	M-M4	M-L2	M-L4	M-C2	M-C4	M-OPC
Chloride migration coefficient ($\times 10^{-12}$ m^2/s)	5.42	4.68	4.55	5.81	4.49	4.11	2.88	7.55

the increasing content of LDH. The slight increase in the M-L2 coefficient is possibly due to the high applied voltage during the NSSM test. Spiesz et al. [52] reported that the coefficient D_{nssm} was nearly 10% larger for samples under the 60 V than the samples under the lower voltages (35 V and 47.5 V). Generally, the dosage of the nitrate intercalated LDH has a direct influence on the chloride resistance of the AAFS matrix, Fig. 17 shows that the chloride resistance of samples is sensitively related to the increasing LDH dosage.

The CLDH incorporation has the highest contribution to chloride binding capacity in the AAFS matrix as shown in Fig. 16 and Fig. 17. The coefficient of M-C2 and M-C4 is lower than M-A0 at 24.2% and 46.9%, respectively. Obviously, the CLDH illustrates the higher chloride resistance than the MgO and LDH addition. This phenomenon may be attributed to the filler effect of LDH formation from CLDH on the AAFS mortars, and the microstructures also prove that the mesopores and macropores decrease as the CLDH content increased. Meanwhile, the mesopores and macropores results are consistent with the observed chloride penetrations in the AAFS matrix. The CLDH addition in AAFS has the lowest mesopores and macropores, thus CLDH contributes to the highest chloride resistance in all the AAFS samples in this study.

The porosity of the samples shows relatively close value (see section 3.3), thus the chloride binding capacity of AAFS samples and OPC samples is predominated by the chemical absorption. The secondary reaction product of AAMs, LDH, induces the main influence. The LDH reconstruction of CLDH has high effectiveness, and LDH addition directly affects the chloride binding capacity. While the MgO has relatively complex process to form LDH in AAMs. Thus, the CLDH admixture shows the highest chloride binding capacity, LDH admixture has moderate chloride resistance, and MgO admixture has the lowest effectiveness in chloride resistance.

4. Conclusions

In this paper, the reaction heat flow, reaction products, microstructure, compressive strength and chloride resistance of alkali activated fly ash and slag blends with the addition of MgO, LDH and CLDH are studied. The different effects of the MgO, Mg-Al-NO_3 LDH and CLDH incorporation are evaluated. The three admixtures in AAFS are proved to enhance the mechanical property, chloride resistance, and microstructure. According to the experimental results, the following conclusions can be drawn:

- The MgO, LDH and CLDH admixtures delay the time to reach the reaction peak (TRRP) in the AAMs matrix up to 3.9%, 11.2%, and 9.2%, respectively. The MgO admixture first forms $Mg(OH)_2$ precipitation, while the Mg-Al-NO_3 LDH and CLDH absorb the OH^-. Therefore, all three admixtures slightly decrease the pH value in the AAFS matrix, and prolong the time to the reaction peak (TTRP).
- MgO promotes the formation of the in-situ growth of LDH phase. The CLDH completes the LDH-reconstruction process in AAFS, during the LDH-reconstruction process, the pH decreases with the consumption of OH^- by CLDH. Meanwhile, the externally added Mg-Al-NO_3 LDH remains in the AAFS matrix. The LDHs phase influenced by the three admixtures shows the partial carbonation in the AAFS matrix, and the carbonation results in the shift of LDH-NO_3 characteristic peak from 11.6° to 13.6°.
- The microstructures of AAFS are refined by the inner filler effect with unreacted MgO. The MgO shows the highest refinement on mesopores and macropores. While the Mg-Al-NO_3 LDH and CLDH admixtures have a limited effect on the microstructure.
- The increased MgO and CLDH content result in the higher compressive strength in AAFS, which is related to the mesopores refinement. While the LDH admixture shows limited influence on the compressive strength.
- MgO, Mg-Al-NO_3 LDH, and CLDH improved the chloride resistance of the AAFS matrix. The CLDH shows the highest chloride binding capacity and enhancement.

CRediT authorship contribution statement

Tao Liu: Methodology, Investigation, Data curation, Formal analysis, Writing - original draft. **Yuxuan Chen:** Investigation, Writing - review & editing. **Qingliang Yu:** Conceptualization, Supervision, Project administration, Writing - review & editing. **Jianfeng Fan:** Writing - review & editing. **H.J.H. Brouwers:** Supervision, Writing - review & editing.

Declaration of Competing Interest

The authors declare that they have no known competing financial interests or personal relationships that could have appeared to influence the work reported in this paper.

Acknowledgments

This study is supported by the China Scholarship Council (Grant No. 201907720114) and Eindhoven University of Technology.

References

[1] C. Tennakoon, A. Shayan, J.G. Sanjayan, A. Xu, Chloride ingress and steel corrosion in geopolymer concrete based on long term tests, Mater. Des. 116 (2017) 287–299, https://doi.org/10.1016/j.matdes.2016.12.030.
[2] J. Osio-Norgaard, J.P. Gevaudan, W.V. Srubar, A review of chloride transport in alkali-activated cement paste, mortar, and concrete, Constr. Build. Mater. 186 (2018) 191–206, https://doi.org/10.1016/j.conbuildmat.2018.07.119.
[3] G. Koch, Cost of corrosion, Trends Oil Gas Corros Res. Technol. Prod. Transm. (2017) 3–30, https://doi.org/10.1016/B978-0-08-101105-8.00001-2.
[4] M. Chi, Effects of dosage of alkali-activated solution and curing conditions on the properties and durability of alkali-activated slag concrete, Constr. Build. Mater. 35 (2012) 240–245, https://doi.org/10.1016/j.conbuildmat.2012.04.005.
[5] S.A. Bernal, R. Mejía De Gutiérrez, J.L. Provis, Engineering and durability properties of concretes based on alkali-activated granulated blast furnace slag/metakaolin blends, Constr. Build. Mater. 33 (2012) 99–108, https://doi.org/10.1016/j.conbuildmat.2012.01.017.
[6] K. Behfarnia, M. Rostami, Effects of micro and nanoparticles of SiO2 on the permeability of alkali activated slag concrete, Constr. Build. Mater. 131 (2017) 205–213, https://doi.org/10.1016/j.conbuildmat.2016.11.070.
[7] R.J. Thomas, E. Ariyachandra, D. Lezama, S. Peethamparan, Comparison of chloride permeability methods for Alkali-Activated concrete, Constr. Build. Mater. 165 (2018) 104–111, https://doi.org/10.1016/j.conbuildmat.2018.01.016.
[8] H.N. Yoon, S.M. Park, H.K. Lee, Effect of MgO on chloride penetration resistance of alkali-activated binder, Constr. Build. Mater. 178 (2018) 584–592, https://doi.org/10.1016/j.conbuildmat.2018.05.156.
[9] C. Monticelli, M.E. Natali, A. Balbo, C. Chiavari, F. Zanotto, S. Manzi, M.C. Bignozzi, A study on the corrosion of reinforcing bars in alkali-activated fly ash mortars under wet and dry exposures to chloride solutions, Cem. Concr. Res. 87 (2016) 53–63, https://doi.org/10.1016/j.cemconres.2016.05.010.
[10] I. Ismail, S.A. Bernal, J.L. Provis, R. San Nicolas, D.G. Brice, A.R. Kilcullen, S. Hamdan, J.S.J. Van Deventer, Influence of fly ash on the water and chloride permeability of alkali-activated slag mortars and concretes, Constr. Build. Mater. 48 (2013) 1187–1201, https://doi.org/10.1016/j.conbuildmat.2013.07.106.
[11] M. Babaee, A. Castel, Chloride diffusivity, chloride threshold, and corrosion initiation in reinforced alkali-activated mortars: Role of calcium, alkali, and silicate content, Cem. Concr. Res. 111 (2018) 56–71, https://doi.org/10.1016/j.cemconres.2018.06.009.
[12] A. Noushini, A. Castel, J. Aldred, A. Rawal, Chloride diffusion resistance and chloride binding capacity of fly ash-based geopolymer concrete, Cem. Concr. Compos. 103290 (2019), https://doi.org/10.1016/j.cemconcomp.2019.04.006.
[13] P.S. Mangat, O.O. Ojedokun, Bound chloride ingress in alkali activated concrete, Constr. Build. Mater. 212 (2019) 375–387, https://doi.org/10.1016/j.conbuildmat.2019.03.302.
[14] D. Bondar, M. Basheer, S. Nanukuttan, Suitability of alkali activated slag/fly ash (AA-GGBS/FA) concretes for chloride environments: characterisation based on mix design and compliance testing, Constr. Build. Mater. 216 (2019) 612–621, https://doi.org/10.1016/j.conbuildmat.2019.05.043.

[15] D. Ravikumar, N. Neithalath, Electrically induced chloride ion transport in alkali activated slag concretes and the influence of microstructure, Cem. Concr. Res. 47 (2013) 31–42, https://doi.org/10.1016/j.cemconres.2013.01.007.

[16] X. Ke, S.A. Bernal, O.H. Hussein, J.L. Provis, Chloride binding and mobility in sodium carbonate-activated slag pastes and mortars, Mater. Struct. Constr. 50 (2017), https://doi.org/10.1617/s11527-017-1121-8.

[17] X. Hu, C. Shi, Z. Shi, L. Zhang, WITHDRAWN: Compressive strength, pore structure and chloride transport properties of alkali-activated slag/fly ash mortars, Cem. Concr. Compos. (2019), https://doi.org/10.1016/j.cemconcomp.2019.01.010.

[18] G. Li, X. Zhang, J. Sun, A. Zhang, C. Liao, Effective removal of bisphenols from aqueous solution with magnetic hierarchical rattle-like Co/Ni-based LDH, J. Hazard. Mater. 381 (2020), https://doi.org/10.1016/j.jhazmat.2019.120985 120985.

[19] J.L. Provis, J.S.J. Van Deventer, Introduction to geopolymers, Geopolymers Struct Process. Prop. Ind. Appl. (2009) 1–11, https://doi.org/10.1533/9781845696382.1.

[20] D.G. Costa, A.B. Rocha, W.F. Souza, S.S.X. Chiaro, A.A. Leitão, Comparative Structural, thermodynamic and electronic analyses of Zn-Al-A n- hydrotalcite-like compounds (A n-Cl -, F -, Br -, OH -, CO 32- or NO 3-: An ab initio study, Appl. Clay Sci. 56 (2012) 16–22, https://doi.org/10.1016/j.clay.2011.11.014.

[21] J. Xu, Y. Song, Y. Zhao, L. Jiang, Y. Mei, P. Chen, Chloride removal and corrosion inhibitions of nitrate, nitrite-intercalated Mg–Al layered double hydroxides on steel in saturated calcium hydroxide solution, Appl. Clay Sci. 163 (2018) 129–136, https://doi.org/10.1016/j.clay.2018.07.023.

[22] Z.Y. Qu, Q.L. Yu, H.J.H. Brouwers, Relationship between the particle size and dosage of LDHs and concrete resistance against chloride ingress, Cem. Concr. Res. 105 (2018) 81–90, https://doi.org/10.1016/j.cemconres.2018.01.005.

[23] D. Tichit, G. Layrac, C. Gérardin, Synthesis of layered double hydroxides through continuous flow processes: a review, Chem. Eng. J. 369 (2019) 302–332, https://doi.org/10.1016/j.cej.2019.03.057.

[24] M. Ben Haha, B. Lothenbach, G. Le Saout, F. Winnefeld, Influence of slag chemistry on the hydration of alkali-activated blast-furnace slag — Part I: Effect of MgO, Cem. Concr. Res. 41 (2011) 955–963, https://doi.org/10.1016/j.cemconres.2011.05.002.

[25] Y. Chen, Z. Shui, W. Chen, G. Chen, Chloride binding of synthetic Ca-Al-NO3 LDHs in hardened cement paste, Constr. Build. Mater. 93 (2015) 1051–1058, https://doi.org/10.1016/j.conbuildmat.2015.05.047.

[26] L. El Gaini, M. Lakraimi, E. Sebbar, A. Meghea, M. Bakasse, Removal of indigo carmine dye from water to Mg-Al-CO3-calcined layered double hydroxides, J. Hazard. Mater. 161 (2009) 627–632, https://doi.org/10.1016/j.jhazmat.2008.04.089.

[27] T. Sato, T. Wakabayashi, M. Shlmada, Adsorption of various anions by magnesium aluminum oxide of (Mg0.7Al0.3O1.15), Ind. Eng. Chem. Prod. Res. Dev. 25 (1986) 89–92, https://doi.org/10.1021/i300021a020.

[28] X. Ke, S.A. Bernal, J.L. Provis, Controlling the reaction kinetics of sodium carbonate-activated slag cements using calcined layered double hydroxides, Cem. Concr. Res. 81 (2016) 24–37, https://doi.org/10.1016/j.cemconres.2015.11.012.

[29] M.A. Shand, The chemistry and technology of magnesia, Chem. Technol. Magnesia (2006) 1–266, https://doi.org/10.1002/0471980579.

[30] EN 196-3, En 196-1, 2005, 1–33.

[31] Influence of pozzolans and slag on the microstructure of partially carbonated cement paste by means of water vapour and nitrogen sorption experiments and BET calculations, Cem. Concr. Res. 40 (2010) 1723–1733. doi:10.1016/j.cemconres.2010.08.014.

[32] NORDTEST, NT Build 492, Nordtest. Proj. 1388, 1999, 1–8.

[33] K. Barlos, D. Gatos, J. Kallitsis, G. Papaphotiu, P. Sotiriu, Y. Wenging, W. Schäfer, Geopolymers and geopolymeric materials, Tetrahedron Lett. 30 (1989) 3943–3946, https://doi.org/10.1190/segam2013-0137.1.

[34] J. Davidovits, Geopolymers – inorganic polymeric new materials, J. Therm. Anal. 37 (1991) 1633–1656, https://doi.org/10.1007/BF01912193.

[35] M. Ben Haha, B. Lothenbach, G. Le Saout, F. Winnefeld, Influence of slag chemistry on the hydration of alkali-activated blast-furnace slag – Part II: Effect of Al2O3, Cem. Concr. Res. 42 (2012) 74–83, https://doi.org/10.1016/j.cemconres.2011.08.005.

[36] X. Ke, S.A. Bernal, J.L. Provis, Uptake of chloride and carbonate by Mg-Al and Ca-Al layered double hydroxides in simulated pore solutions of alkali-activated slag cement, Cem. Concr. Res. 100 (2017) 1–13, https://doi.org/10.1016/j.cemconres.2017.05.015.

[37] Z. Ali, I. Khan, I. Ahmad, M.S. Khan, S.J. Asadabadi, Mater. Chem. Phys. 3 (2015) 1–8, https://doi.org/10.1016/j.matchemphys.2015.05.072.

[38] G. Liu, M.V.A. Florea, H.J.H. Brouwers, Waste glass as binder in alkali activated slag–fly ash mortars, Mater. Struct. 52 (2019), https://doi.org/10.1617/s11527-019-1404-3.

[39] F. Moghaddam, V. Sirivivatnanon, K. Vessalas, The effect of fly ash fineness on heat of hydration, microstructure, flow and compressive strength of blended cement pastes, Case Stud. Constr. Mater. 10 (2019), https://doi.org/10.1016/j.cscm.2019.e00218.

[40] K. Kiattikomol, C. Jaturapitakkul, S. Songpiriyakij, S. Chutubtim, A study of ground coarse fly ashes with different finenesses from various sources as pozzolanic materials, Cem. Concr. Compos. 23 (2001) 335–343, https://doi.org/10.1016/S0958-9465(01)00016-6.

[41] F. Jin, K. Gu, A. Al-Tabbaa, Strength and drying shrinkage of reactive MgO modified alkali-activated slag paste, Constr. Build. Mater. 51 (2014) 395–404, https://doi.org/10.1016/j.conbuildmat.2013.10.081.

[42] F. Jin, K. Gu, A. Al-Tabbaa, Strength and hydration properties of reactive MgO-activated ground granulated blastfurnace slag paste, Cem. Concr. Compos. 57 (2015) 8–16, https://doi.org/10.1016/j.cemconcomp.2014.10.007.

[43] C.L. Hwang, D.H. Vo, V.A. Tran, M.D. Yehualaw, Effect of high MgO content on the performance of alkali-activated fine slag under water and air curing conditions, Constr. Build. Mater. 186 (2018) 503–513, https://doi.org/10.1016/j.conbuildmat.2018.07.129.

[44] P. Duan, W. Chen, J. Ma, Z. Shui, Influence of layered double hydroxides on microstructure and carbonation resistance of sulphoaluminate cement concrete, Constr. Build. Mater. 48 (2013) 601–609, https://doi.org/10.1016/j.conbuildmat.2013.07.049.

[45] Y. Chen, R. Yu, X. Wang, J. Chen, Z. Shui, Evaluation and optimization of Ultra-High Performance Concrete (UHPC) subjected to harsh ocean environment: towards an application of Layered Double Hydroxides (LDHs), Constr. Build. Mater. 177 (2018) 51–62, https://doi.org/10.1016/j.conbuildmat.2018.03.210.

[46] S.A. Bernal, R. San Nicolas, R.J. Myers, R. Mejía De Gutiérrez, F. Puertas, J.S.J. Van Deventer, J.L. Provis, MgO content of slag controls phase evolution and structural changes induced by accelerated carbonation in alkali-activated binders, Cem. Concr. Res. 57 (2014) 33–43, https://doi.org/10.1016/j.cemconres.2013.12.003.

[47] Y. Chen, Z. Shui, W. Chen, Q. Li, G. Chen, Effect of MgO content of synthetic slag on the formation of Mg-Al LDHs and sulfate resistance of slag-fly ash-clinker binder, Constr. Build. Mater. 125 (2016) 766–774, https://doi.org/10.1016/j.conbuildmat.2016.08.086.

[48] C. Shi, Effect of mixing proportions of concrete on its electrical conductivity and the rapid chloride permeability test (ASTM C1202 or ASSHTO T277) results, Cem. Concr. Res. 34 (2004) 537–545.

[49] J.C. Liu, T.J. Wang, L.C. Sung, P.F. Kao, T.Y. Yang, W.R. Hao, C.C. Chen, Y.P. Hsu, S.Y. Wu, Influenza vaccination reduces hemorrhagic stroke risk in patients with atrial fibrillation: a population-based cohort study, Int. J. Cardiol. 232 (2017) 315–323, https://doi.org/10.1016/j.ijcard.2016.12.074.

[50] G. Liu, M.V.A. Florea, H.J.H. Brouwers, Characterization and performance of high volume recycled waste glass and ground granulated blast furnace slag or fly ash blended mortars, J. Clean. Prod. 235 (2019) 461–472, https://doi.org/10.1016/j.jclepro.2019.06.334.

[51] M. Babaee, A. Castel, Water vapor sorption isotherms, pore structure, and moisture transport characteristics of alkali-activated and Portland cement-based binders, Cem. Concr. Res. 113 (2018) 99–120, https://doi.org/10.1016/j.cemconres.2018.07.006.

[52] P. Spiesz, H.J.H. Brouwers, Influence of the applied voltage on the Rapid Chloride Migration (RCM) test, Cem. Concr. Res. 42 (2012) 1072–1082, https://doi.org/10.1016/j.cemconres.2012.04.007.